IEEE Access
Multidisciplinary ⋮ Rapid Review ⋮ Open Access Journal

Received January 18, 2022, accepted February 4, 2022, date of publication February 8, 2022, date of current version March 23, 2022.

Digital Object Identifier 10.1109/ACCESS.2022.3150095

Q-Band Radial Waveguide Power Divider Based on a Specific Cycloidal-Like Transition Implementation

FEI LIANG, JIAQUAN YE, YUANKAI LI, HUAN LIN, BIN YUAN, AND JIAN XU
Second Research Institute of CAAC, Chengdu 610041, China

Corresponding author: Jiaquan Ye (yejq@caacsri.com)

This work was supported in part by the 2021 Civil Aviation Administration of China Security Capability Project "Research and Validation of Lightweight Metamaterials to Mitigate the Impact of Large Airport Buildings on Localizer Signals."

ABSTRACT An axially symmetric radial waveguide power divider, which utilizes a specific Cycloidal-Like tapered transition between a central coaxial launcher and a radial waveguide, is presented in this paper. In order to broad the operation band, the change of impedance of the coaxial to radial waveguide transition is investigated, and an analytic expression for the shape of the transition is obtained. A simple electromagnetic modeling for the stepped radial matching network is developed, and its characteristics are analyzed in detail using the circuit method. Eventually, a stepped-by-stepped design procedure for the power divider is established for the design of the radial waveguide power divider. A twenty-way radial waveguide divider is designed, fabricated, and measured to validate the proposed method. The measurements show that the return loss at the input port is better than 20 dB over almost the full *Q*-band (33 to 48 GHz), while the amplitude/phase imbalance are within ±0.5 dB and ±3°, respectively. The simulated and measured results demonstrate a high degree of agreement.

INDEX TERMS Broadband, coaxial waveguide, power divider, radial waveguide, taper transition.

I. INTRODUCTION

Recently, due to the rapid advancements of military and commercial communication systems, there are increasingly demand for broadband microwave and millimeter-wave high-power solid-state amplifiers. Nevertheless, it is difficult for the existing semiconductor technology to achieve a high power levels that satisfy the system demand by an individual solid-state device. Therefore, it is necessary to combine the power of numerous devices efficiently to obtain a desired output power [1], [2].

Various topologies of waveguide quasi-planar (e.g., waveguide T-junction, waveguide traveling wave power divider) circuits have been recently proposed and have proved their effectiveness in systems such as power amplifier modules, antenna arrays, etc. [3]–[8]. However, it has to be admitted that these configurations also have some unavoidable limitations, which are determined by the inherent characteristics. For example, conventional tree-type combiners and chain-type combiners are not suitable for multiplexed distribution, due to the long transmission paths that would lead to ultra-high losses. In addition, the bulky device size also limits its applications. In order to overcome these drawbacks, radial power combiners have been developed and widely investigated. It can be designed based on various transmission waveguides that are axially symmetric, such as coaxial waveguides [9]–[14], radial waveguides [15]–[22], conical waveguides [23]–[26], and circular waveguides [27]. Owing to the inherent circularly symmetric configuration and the advantage of single-step synthesis, radial combiners have low losses, compact dimensions, and better amplitude and phase balance (compared to binary power dividers).

Generally, a coaxial or circular waveguide providing a circumferentially symmetric EM field excitation for the radial power divider is the recommended solution. This is due to the fact that the operating modes of these configurations do not shift with angle and are quite accessible, such as the TE01 mode in circular waveguides [27], or TM01 [28], and the TEM mode in coaxial waveguides [29]. Then, the

The associate editor coordinating the review of this manuscript and approving it for publication was Chenghong Gu.

critical element for high-performance radial combiners is the design of efficient transitions from these types of input configurations to radial waveguides, which must contain broadband characteristics, as well as robustness. Some solutions for transitions have been reported, for example, in [24], an X-band ten-way combiner with a constant impedance transformed coaxial-tapered waveguide transition was designed. The measured results show that the proposed structure achieves 74% bandwidth with a return loss better than 14.7 dB. In [10], a variety of coaxial structure combiners with a tapered impedance transition are proposed with a measured reflection coefficient of −15 dB covering and bandwidth of 28% (center frequency of 14 GHz). In addition, a general coaxial-tapered transmission line transition solution is presented in [14] with a built-in impedance taper that can be explicitly selected. It provides more freedom and greater flexibility for impedance transformation between tapered and differently sized coaxial lines. The method was validated with a fabricated eight-way combiner with a measured reflection coefficient better than −22 dB in the frequency range from 1.5 GHz to 5.5 GHz. It is certain that these radial combiners all obtain a wide bandwidth, however, they are all based on coaxial or microstrip as output, which limits the power capacity of the device to some extent. Moreover, all these transitions operate only in the lower bands (S, C-band [14], X-band [10], [24]). For the millimeter band (over 30 GHz), the investigation of impedance tapering structures with high robustness is urgently needed because of the dramatic shrinkage of the device size.

In this paper, a solution for radial power distribution based on cycloidal impedance matching transition is proposed in order to extend the application scenario of radial architecture. The proposed new transition structure not only offers broadband advantages, but is also shown to be insensitive to dimensional changes. Completely, detailed design procedure for the transition profile is given. Finally, a twenty-way radial power combiner is designed and fabricated to validate the proposed solution. Experimental results show that the device demonstrates excellent performance in the frequency range from 33 to 48 GHz (Q-band), including low loss, wide bandwidth, etc., thus being potentially valuable in multi-way synthesis devices.

Rest of the papers is organized as follows: the detailed deduced procedures of the transition is introduced in Section II. Based on the obtained transition, a Q-band twenty-way radial waveguide power divider with a standard rectangular waveguide input/ouput is developed in Section III. Considering that the dispersive environment of the rectangular waveguide and the problem of radial waveguide that the characteristic impedance against radial distance, a stepped radial matching network is adopted to achieve a wide-band impedance matching between the radial waveguide input and the N rectangular waveguide. The experimental results are detailed in Section IV. Finally, a brief conclusion is given in Section V.

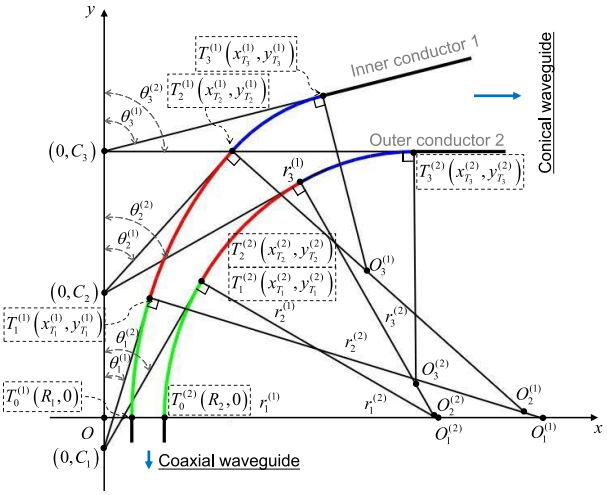

FIGURE 1. Profile sketch of a multi-section coaxial to conical waveguide transition with $K = 3$. The first section is colored green, the second section is colored red, and the third section is colored blue. Each section arc radii remain constant from the starting to the ending.

II. DESIGN PROCEDURE FOR CYCLOIDAL-LIKE IMPEDANCE TAPER TRANSITION

In general, to achieve broadband matching as well as high power capacity, the coaxial-to-radial waveguide transition section should preferably have a smooth profile and an easily controllable impedance value. The proposed transition is decomposed into two parts, the coaxial to conical waveguide transition, and the conical to radial waveguide connection part, respectively. A detailed profile of the former is shown in Fig. 1, which is divided into K different arcs ($K = 3$ is presented as an example in Fig. 1 for clarity).

Each *k-th* section is a smooth arc which remains a constant radii from the start to the end. In addition, the adjacent sections of the conductor are required that the geometry must remain smooth within the transition. The joint points of the K sections divide the transition into $K + 1$ discrete impedance levels which can be viewed as the conical transmission lines with the starting angle ($\theta_k^{(1)}$), and the ending angle ($\theta_k^{(2)}$), $k = 0, 1, \ldots, K$ [(1), (2) refer to the inner conductor and the outer conductor of the transition, respectively]. When $k = 0$, the impedance of the conical waveguide ($\theta_0^{(1)} = \theta_0^{(2)} = 0$) is reduced into the starting coaxial waveguide impedance.

For the purpose of subsequent illustration, the implications of some critical parameters are declared here. First note that the angle of $\theta_K^{(2)}$ is 90°, which is determined by the geometry of the transition. Besides, the connection point at the end of the *k-th* segment arc is defined as $T_k^{(c)}$ ($c = 1, 2$). The tangent line of the profile at $T_k^{(c)}$ is defined as $l_k^{(c)}$, and the vertical line of $l_k^{(c)}$ is marked as $\underline{l_k^{(c)}}$. The total length of the transition is considered to be equal to the length of the inner conductor profile (denoted by $S_k^{(1)}$.).

A. DESIGN OF THE 1-ST SECTION

Since the first section of the coaxial to conical waveguide transition is a coaxial waveguide with an inner conductor radii

R1 and an outer conductor radii *R2*, the *1-st* section of the transition is known as $\theta_0^{(1)} = \theta_0^{(2)} = 0$. Therefore, the first section can be determined once the ending angle $\theta_1^{(1)}$ and $\theta_1^{(2)}$ are known. Considering that $\theta_1^{(1)}$ and $\theta_1^{(2)}$ are associated with the conical waveguide characteristic impedance, an initial value for $\theta_1^{(1)}$ is assumed. Then, $r_1^{(1)}$ is determined as follows:

$$r_1^{(1)} = \frac{S_1^{(1)}}{\theta_1^{(1)}}. \tag{1}$$

The impedance level Z_k of the *k-th* section is calculated using the conical waveguide characteristic impedance:

$$Z_k = 60ln\frac{tan(\theta_k^{(2)}/2)}{tan(\theta_k^{(1)}/2)}. \tag{2}$$

Therefore, $\theta_1^{(2)}$ can be determined when a desired impedance Z_1 is given, as:

$$\theta_1^{(2)} = 2arctan[tan(\theta_1^{(1)}/2)e^{(Z_1/60)}]. \tag{3}$$

For the first arc of the transition, the center of the arcs must be located at the x-axis. Then, the central coordinates $O_1^{(1)}$ and the connection point $T_1^{(1)}$ of the inner conductor can be determined as:

$$O_1^{(1)} = (x_1^{(1)}, y_1^{(1)}) = (r_1^{(1)} + R_1, 0) \tag{4}$$

$$T_1^{(1)} = (x_{T_1}^{(1)}, y_{T_1}^{(1)}) = (R_1 + 2r_1^{(1)}sin^2(\theta_1^{(1)}/2), r_1^{(1)}sin\theta_1^{(1)}). \tag{5}$$

Based on the above, if $\theta_1^{(1)}$ is given, then the expression of C_1 can be determined using (5).

$$C_1 = y_{T_1}^{(1)} - x_{T_1}^{(1)}tan(\pi/2 - \theta_1^{(1)}). \tag{6}$$

Furthermore, according to the geometric relations of this transition, it can be seen that the center coordinate of the outer conductor satisfy the following equation:

$$\left|x_1^{(2)} - R_2\right| = \frac{\left|x_1^2 tan(\pi/2 - \theta_1^{(2)}) + C_1\right|}{\sqrt{tan^2(\pi/2 - \theta_1^{(2)}) + 1}}. \tag{7}$$

Therefore, integrate (5)-(7), the value of $r_1^{(2)}$ can be determined. Note that (7) has two roots, while only $x_1^{(2)} > R_2$ is the desired one since $O_1^{(2)}$ must locate at the right side of $T_0^{(2)}$.

$$r_1^{(2)} = x_1^{(2)} - R_2 \tag{8}$$

Analogously, the ending point $T_1^{(2)}$ of the *1-st* section arc of the outer conductor is given as:

$$T_1^{(2)} = (x_{T_1}^{(2)}, y_{T_1}^{(2)}) = (R_2 + 2r_1^{(2)}sin^2(\theta_1^{(2)}/2), r_1^{(2)}sin\theta_1^{(2)}). \tag{9}$$

Hence, it can be seen that all the parameters of the *1-st* section are deduced according to the (1)–(9) if the value of $\theta_1^{(1)}$, Z_1 and $S_1^{(1)}$ are specified.

B. DESIGN OF THE K-TH SECTION

Based on the above analysis, the relationship between $\theta_k^{(1)}$ and $\theta_k^{(2)}$ has been obtained. Then, the entire profile of the coaxial to conical waveguide transition will be traced, simply by determining either of these two values. Since $\theta_k^{(2)}$ can only take values in the range of 0° to 90°, it is easier to determine its initial value than $\theta_k^{(1)}$, which can be written specifically as

$$\theta_k^{(2)} = \theta_1^{(2)} + \frac{\pi/2 - \theta_1^{(2)}}{K - 1}(k - 1). \tag{10}$$

Then, (2) can be rewritten as (11) to obtain the value of $\theta_k^{(1)}$ if the desired Z_k is given.

$$\theta_k^{(1)} = 2arctan[\frac{tan(\theta_k^{(2)}/2)}{e^{(Z_k/60)}}]. \tag{11}$$

Using the value of $\theta_k^{(1)}$ as well as the given length $S_k^{(1)}$ of the transition, the *k-th* section arc radii of inner conductor is deduced as

$$r_k^{(1)} = \frac{S_k^{(1)}}{\theta_k^{(1)} - \theta_{k-1}^{(1)}}. \tag{12}$$

Since the distance from the $O_k^{(1)}$ to $T_{k-1}^{(1)}$ is equal to the radii $r_k^{(1)}$, the center coordinate $O_k^{(1)}(x_k^{(1)}, y_k^{(1)})$ should satisfy the following equations:

$$\sqrt{(x_k^{(1)} - x_{T_{k-1}}^{(1)})^2 + (y_k^{(1)} - y_{T_{k-1}}^{(1)})^2} = r_k^{(1)} \tag{13}$$

$$x_k^{(1)} > x_{T_{k-1}}^{(1)}, \quad y_k^{(1)} > y_{T_{k-1}}^{(1)}. \tag{14}$$

where $x_{T_{k-1}}^{(1)}$ and $y_{T_{k-1}}^{(1)}$ are the ending point coordinates of the *(k-1)-th* section arc of the inner conductor. However, the values of $x_k^{(1)}$ and $y_k^{(1)}$ are not completely determined by (13) and (14), thus an additional condition should be added.

Since the point $O_k^{(1)}$ lain on the line $\overline{l_{k-1}^{(1)}}$, the follow equation could be obtained.

$$y_k^{(1)} = x_k^{(1)}tan(\pi - \theta_{k-1}^{(1)}) + b_{k-1}^{(1)}, \tag{15}$$

where

$$b_{k-1}^{(1)} = y_{T_{k-1}}^{(1)} - x_{T_{k-1}}^{(1)}tan(\pi - \theta_{k-1}^{(1)}). \tag{16}$$

Therfore, according to (13)-(16), the coordinate of $O_k^{(1)}(x_k^{(1)}, y_k^{(1)})$ can be calculated.

On the other hand, the ending point $T_k^{(1)}(x_{T_k}^{(1)}, y_{T_k}^{(1)})$ of the *k-th* section arc of the inner conductor can also be calculated as follows:

$$x_{T_k}^{(1)} = x_k^{(1)} + 2r_k^{(1)}sin(\frac{\Delta\theta_k^{(1)}}{2})cos(\frac{\pi - \Delta\theta_k^{(1)}}{2} - \theta_{k-1}^{(1)}), \tag{17}$$

$$y_{T_k}^{(1)} = y_k^{(1)} + 2r_k^{(1)}sin(\frac{\Delta\theta_k^{(1)}}{2})sin(\frac{\pi - \Delta\theta_k^{(1)}}{2} - \theta_{k-1}^{(1)}), \tag{18}$$

where

$$\Delta\theta_k^{(1)} = \theta_k^{(1)} - \theta_{k-1}^{(1)}. \tag{19}$$

Based on (10)-(19), the *k-th* section of the inner conductor is uniquely identified once the value of $\theta_k^{(2)}$ is given.

In order to fully define geometry of the transition, the *k-th* section of the outer conductor should be discussed. According to the geometry relationship shown in Fig. 1, the value of C_k is obtained by

$$C_k = y_{T_k}^{(1)} - x_{T_k}^{(1)} tan(\pi/2 - \theta_k^{(1)}). \tag{20}$$

Correspondingly, the line $l_k^{(2)}$ can be also determined. According to the following conditions: (1) the distances of the point $O_k^{(2)}$ to the line $l_k^{(2)}$ and the line $l_{k-1}^{(2)}$ must be equal; (2) the point $O_k^{(2)}$ is located on the line $L_{k-1}^{(2)}$; (3) the point $O_k^{(2)}$ is seated at the upper right of the point $T_{k-1}^{(2)}$, the location of point $O_k^{(2)}$ is determined by following equation:

$$\frac{\left|x_k^{(2)} tan(\pi/2 - \theta_k^{(2)}) + C_k - y_k^{(2)}\right|}{\sqrt{tan^2(\pi/2 - \theta_k^{(2)}) + 1}} = \frac{\left|x_k^{(2)} tan(\pi/2 - \theta_{k-1}^{(2)}) + C_{k-1} - y_{k-1}^{(2)}\right|}{\sqrt{tan^2(\pi/2 - \theta_{k-1}^{(2)}) + 1}}, \tag{21}$$

$$y_k^{(2)} = x_k^{(2)} tan(\pi - \theta_{k-1}^{(2)}) + b_{k-1}^{(2)}, \tag{22}$$

$$x_k^{(2)} > x_{T_{k-1}}^{(2)}, y < y_{T_{k-1}}^{(2)}, \tag{23}$$

where

$$b_{k-1}^{(2)} = y_{k-1}^{(2)} - x_{k-1}^{(2)} tan(\pi - \theta_{k-1}^{(2)}). \tag{24}$$

The *k-th* section arc radii of the outer conductor can be calculated by

$$r_k^{(2)} = \sqrt{(x_k^{(2)} - x_{T_{k-1}}^{(2)})^2 + (y_k^{(2)} - y_{T_{k-1}}^{(2)})^2}. \tag{25}$$

Then, the point $T_k^{(2)}(x_{T_k}^{(2)}, y_{T_k}^{(2)})$ can also be obtain by rewritten (17) and (18), as:

$$x_{T_k}^{(2)} = x_k^{(2)} + 2r_k^{(2)} sin(\frac{\Delta\theta_k^{(2)}}{2}) cos(\frac{\pi - \Delta\theta_k^{(2)}}{2} - \theta_{k-1}^{(2)}) \tag{26}$$

$$y_{T_k}^{(2)} = y_k^{(2)} + 2r_k^{(2)} sin(\frac{\Delta\theta_k^{(2)}}{2}) sin(\frac{\pi - \Delta\theta_k^{(2)}}{2} - \theta_{k-1}^{(2)}) \tag{27}$$

C. DESIGN OF THE LAST SECTION OF THE INNER CONDUCTOR PROFILE

The previous section describes the design process of the cycloidal-like transition from the coaxial waveguide to the conical waveguide. This section will show the second part of the transition, i.e., the connection of the conical waveguide to the radial waveguide. This segment is necessary because the rotation angle of the inner conductor at the output of the conical waveguide is less than 90°, which leads to a non-smooth connection at the end of the transition.

As shown in Fig 2, the conical to radial waveguide connecting section is constructed by a smooth arc (last section), which the radii remain constant from the starting angle $\theta_K^{(1)}$ to the ending angle $\theta_{K+1}^{(1)}$. The ordinate of the ending point $x_{K+1}^{(1)}$ equal to $x_K^{(2)}$. According to the above conditions, the center point of the arc can be given as

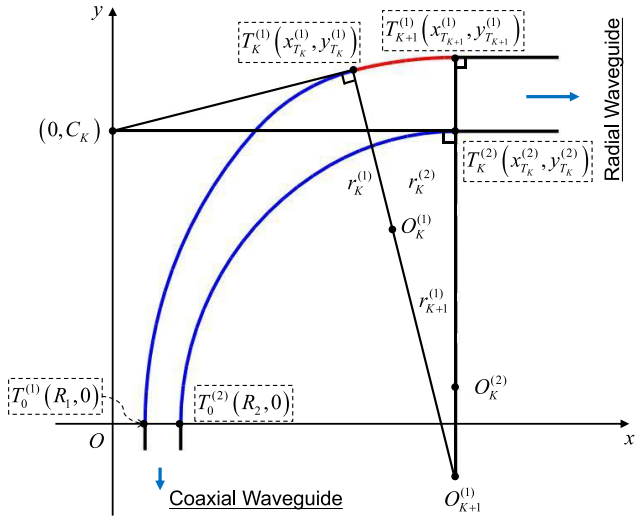

FIGURE 2. Profile sketch of a coaxial to radial waveguide transition. The red arc is is constructed by the proposed method.

$$x_{K+1}^{(1)} = x_K^{(2)}, \tag{28}$$

$$y_{K+1}^{(1)} = x_{K+1}^{(2)} tan(\pi - \theta_K^{(1)}) + b_K^{(1)}, \tag{29}$$

the value of $b_K^{(1)}$ can be deduced from (16).

The radii $r_{K+1}^{(1)}$ and the ending point $T_{K+1}^{(1)}$ of the arc are calculated as follows:

$$r_{K+1}^{(1)} = \sqrt{(x_{K+1}^{(1)} - x_{T_k}^{(1)})^2 + (y_{K+1}^{(1)} - y_{T_k}^{(1)})^2}, \tag{30}$$

$$T_{K+1}^{(1)} = (x_{T_{K+1}}^{(1)}, y_{T_{K+1}}^{(1)}) = (x_K^{(1)}, y_{K+1}^{(1)} + r_{K+1}^{(1)}). \tag{31}$$

Due to the introduction of the last section, the desired output impedance of the coaxial to conical waveguide transition is changed, and the actual output impedance is obtained by the radial line characteristic impedance, as

$$Z_L = \frac{\Delta h}{2\pi r}\sqrt{\frac{\mu}{\varepsilon_r \varepsilon_0}}, \tag{32}$$

where ε_r is the relative permittivity of the dielectric, ε_0 is the permittivity of the vacuum, μ is the permeability of the dielectric, Δh is the height of the radial waveguide, and r is the radial distant. In this case, Δh and r are calculated by

$$\Delta h = y_{T_{k+1}}^{(1)} - y_{T_k}^{(2)}, \tag{33}$$

$$r = x_{T_k}^{(2)}. \tag{34}$$

In fact, the value of Z_L and Z_K are only slightly different while the angle $\theta_K^{(1)}$ is closes to 90° (has a low level). Therefore, if Z_L in (32) is substituted by Z_K, the output height can be controlled by adjusting the value of $x_{T_k}^{(2)}$, which is determined by the value of $\theta_1^{(1)}$ and $\theta_k^{(2)}$.

D. SUMMARY OF THE DESIGN PROCEDURE FOR THE COAXIAL TO RADIAL WAVEGUIDE TRANSITION

From (1)-(34), it is clearly that the shape of the transition can be fully defined if the value of $\theta_1^{(1)}$ and $\theta_k^{(2)}$ are known. However, the shape of transition is not unique according to the impedance profile since of the value of $\theta_1^{(1)}$ and $\theta_k^{(2)}$ aren't unique. In fact, the majority of these transition isn't coincident with the desired impedance profile. The reason is that the *k-th* section arc length of the outer conductor is determined by the value of $\theta_1^{(1)}$ and $\theta_k^{(2)}$, and usually isn't equal to the desired length. Hence, an optimization algorithm is proposed to obtain the value of $\theta_1^{(1)}$ and $\theta_k^{(2)}$,and the goal is to minimize the follow error function:

$$\Delta\gamma = \sum_{k=1}^{M} (S_k^{(1)} - r_k^{(2)} \Delta\theta_k^{(2)})^2, \tag{35}$$

the value of $\theta_1^{(1)}$ and $\theta_k^{(2)}$ are the optimization parameters.

Based on the above discussion, the design procedure of the coaxial to radial transition is summarized as follows.

1) Choose an initial value for $\theta_1^{(1)}$, as well as give the desire Z_k and $S_k^{(1)}$.
2) Set $k = 1$, calculate the *1-st* section of the transition using (1)-(9).
3) Calculate the initial $\theta_k^{(2)}$ and $\theta_k^{(1)}$ using (10), (11), and Z_k.
4) Set $k = k + 1$, calculate the *k-th* section of the transition using (12)-(27).
5) Repeat the step 4) until $k = M$.
6) Calculate the last connecting section of the inner conductor profile based on (28)-(34).
7) Use the numerical algorithm to minimize the value of $\Delta\gamma$ by choosing the value of $\theta_1^{(1)}$, and $\theta_k^{(2)}$ repeatedly, and repeat the step 2) to the step 7). Note that (10) is not necessary expect for the first calculation.

III. STRUCTURE AND ANALYSIS OF RADIAL WAVEGUIDE POWER DIVIDER

Based on the aforementioned design method of the coaxial to radial waveguide transition, a *Q*-band twenty-way radial waveguide power divider for is analyzed and designed. The sketch of the proposed radial waveguide power divider is depicted in Fig. 3. The port numbering is shown in Fig. 4. The divider consists of four sections, i.e: 1) the rectangular to coaxial waveguide transition; 2) the impedance tapered coaxial to radial waveguide transition; 3) the stepped radial matching network; and 4) the N output rectangular ports.

The input and output ports are all in standard rectangular waveguide. The N rectangular output ports are placed at periphery of the stepped radial matching network along the radial direction, and the waveguide's E-plane is perpendicular to the central base axil. Besides, the stepped radial matching network can be viewed as a multi-segment radial transmission lines. The height of the network output is consistent with the rectangular waveguide. Finally, the radius of the synthesis

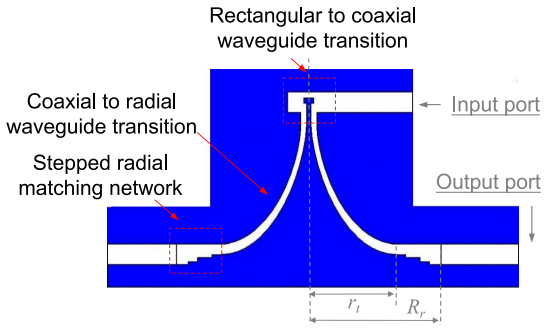

FIGURE 3. Sketch of a broadband radial waveguide power divider using a novel taper transition.

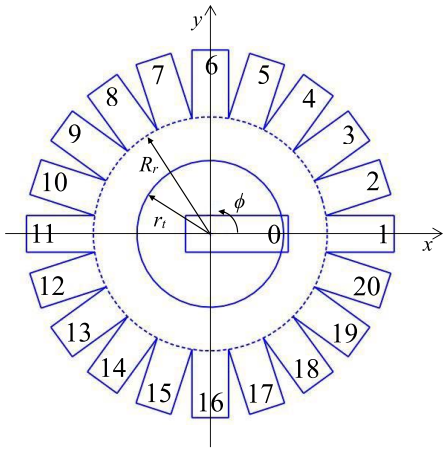

FIGURE 4. Numbering of the ports of a twenty-way power divider/combiner.

network needs to hold N rectangular ports, while also ensuring that it is as small as possible to prevent propagation of higher order modes. And the transition from the coaxial to the radial waveguide is axially symmetric with respect to the central base axis. It is also worth mentioning that each part of the splitter is filled with air.

A. DESIGN EXAMPLE FOR THE COAXIAL-RADIAL WAVEGUIDE TRANSITION

According to the design theory and procedure introduced earlier in Section II, an coaxial to radial waveguide transition, which the inner and outer conductor radii for the coaxial waveguide is fixed to 0.35 mm and 1.1 mm, respectively, is designed. The given tapered impedance profile is shown in Fig. 5. The calculated results of the transition are summarized in Table 1. It should note that the red point is the actual output impedance of the coaxial to radial waveguide transition.

The simulated reflection coefficients based on the ideal transmission line model in the circuit by a given impedance level are shown in Fig. 6. In addition, using the results in Table 1, the simulation results of the 3D electromagnetic model of the coaxial to radial waveguide transition constructed in Ansoft High Frequency Structure Simula-

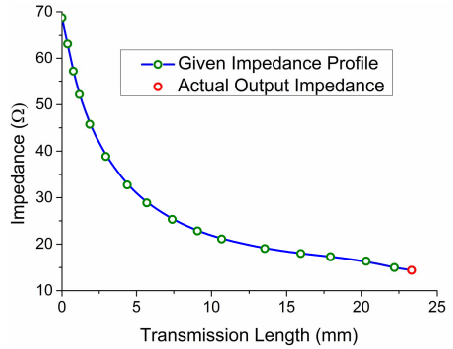

FIGURE 5. Impedance variation curves in the design example (red dots refer to the calculated actual output impedance of the coaxial to radial waveguide transition).

TABLE 1. Calculated information for the example transition.

k	$\theta_k^{(1)}$	$\theta_k^{(2)}$	$r_k^{(1)}$	$r_k^{(2)}$	$x_{T_K}^{(1)}$	$y_{T_K}^{(1)}$	$x_{T_K}^{(2)}$	$y_{T_K}^{(2)}$
0	0	0	/	/	0.35	0	1.1	0
1	3.27	9.35	6.61	9.11	0.36	0.38	1.22	1.48
2	4.7	12.15	15.55	41.65	0.39	0.76	1.6	3.48
3	5.88	13.97	19.85	0	0.43	1.17	1.6	3.48
4	7.54	16.08	23.89	45.15	0.51	1.86	2.03	5.09
5	9.73	18.47	28.13	9.56	0.67	2.92	2.15	5.47
6	12.34	21.14	31.5	39.93	0.94	4.33	2.78	7.22
7	14.62	23.45	33.01	7.11	1.25	5.61	2.89	7.48
8	17.59	26.56	32.85	35.27	1.72	7.24	3.7	9.22
9	20.68	29.89	31.23	9.08	2.27	8.83	3.95	9.68
10	23.87	33.46	28.68	29.32	2.88	10.31	4.9	11.23
11	30.67	41.29	24.13	10.3	4.19	12.86	5.76	12.35
12	38.17	50.06	18.35	16.58	5.55	14.84	7.57	14.12
13	46.51	59.67	13.7	5.13	6.89	16.31	8.27	14.62
14	60.57	74.99	9.73	9.82	8.8	17.72	10.69	15.63
15	75.82	90	7.08	3.82	10.55	18.42	11.68	15.76
last	90	/	4.62	/	11.68	18.56	/	/

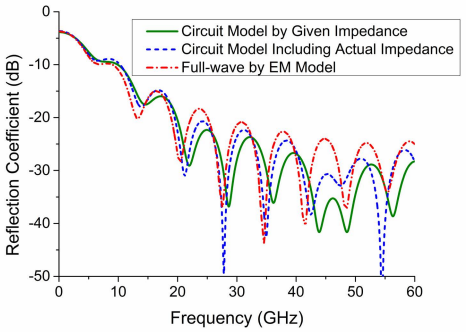

FIGURE 6. Comparision reflection coefficients of circuit model and full-wave simulated.

tor (HFSS) are included in the figure. It can be seen that the curves obtained a highly consistent.

Based on the calculated joint points of each section of the transition in Table 1, the profiles of the inner and outer conductor are fitted by the numerical method. An analytical

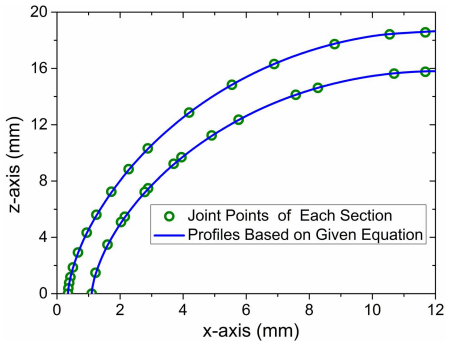

FIGURE 7. Calculated joint points of each section for the transition and the depicted profiles by the given (36).

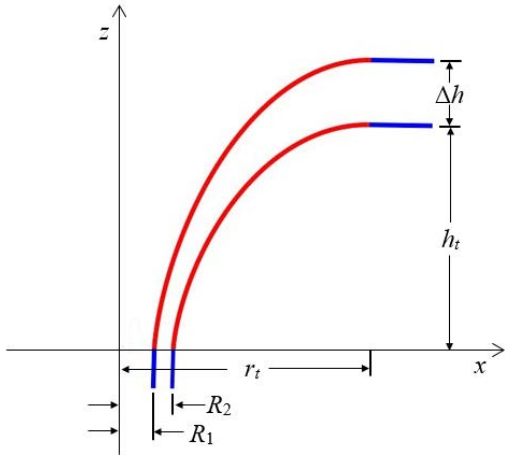

FIGURE 8. Dimensional schematic of the coaxial-radial waveguide tapering transition constructed based on (36).

express of the shape is obtained as follows:

$$\begin{cases} x = \dfrac{r_t - R}{\pi} \left[\dfrac{\pi t}{r_t - R} - \sin\left(\dfrac{\pi t}{r_t - R_1} \right) \right] + R \\ z = \dfrac{h_t}{2} \left[1 - \cos\left(\dfrac{\pi t}{r_t - R} \right) \right], \end{cases} \quad 0 \le t \le r_t - R \tag{36}$$

where r_t is the horizontal radii of the curves, h_t is the vertical height of the curves, and R refer to inner and outer conductor radii of the coaxial waveguide.

In this case, the dimensions of the outer conductor profile are as follows: $r_t = 12$ mm, $R = 1.1$ mm, $h_t = 15.8$ mm. For the inner conductor, $h_t = 18.645$ mm, $R = 0.35$ mm, and keeping the r_t fixed. The comparison between the profiles given by the above equation and the calculated joint points is depicted in Fig 7. Obviously, the given equation agree well with the calculated transition profiles. Therefore, the analytical express of the shape is a universal mode since the profile of the transition is deduced strictly based on the impedance matching theory.

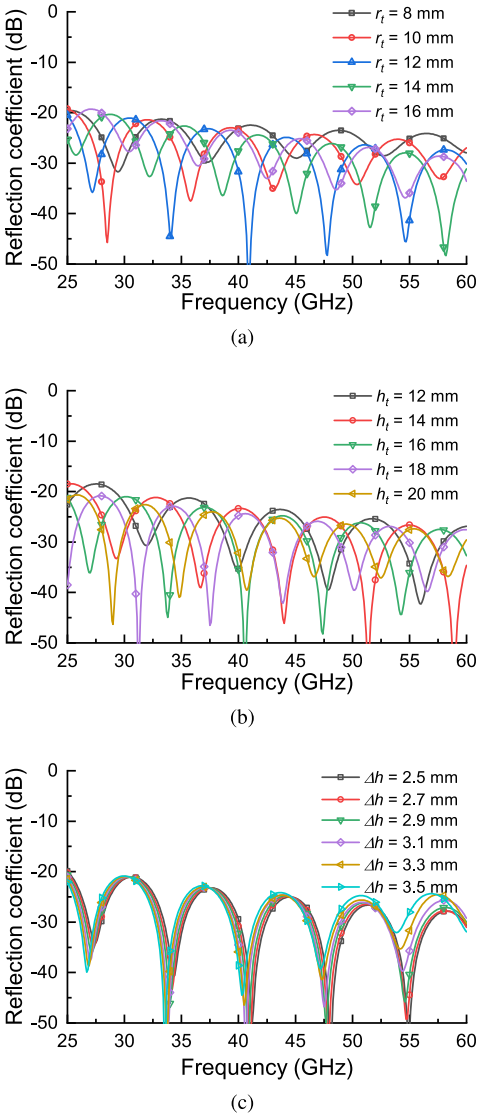

FIGURE 9. Tolerance analysis of the proposed transition (keeping R_1 = 0.35 mm, $R2$ = 1.1 mm). (a) r_t. (b) h_t.(c) Δh.

We have performed a robustness analysis of the proposed coaxial-radial waveguide transition. Some critical dimensions (e.g., r_t, h_t Δh in Fig. 8) were parametrically swept in HFSS to show their effects on the reflection coefficient. The simulation results are shown in Fig. 9, and it can be seen that the proposed transition has a strong tolerance performance. Its input reflection coefficient is insensitive to the variation of physical dimensions. When the length of the transition is selected appropriately, the reflection coefficient can be kept at a lower level (around 20 dB) in the range of 25 to 60 GHz with an assembly error of 10 mm. The above characteristics can reduce the requirement for transition processing accuracy. This is necessary in the millimeter band, because the device size has been shrunk to the mm-level. In addition, the results of these analyses reveal a potential advantage of the transition. Namely, when it is applied to a

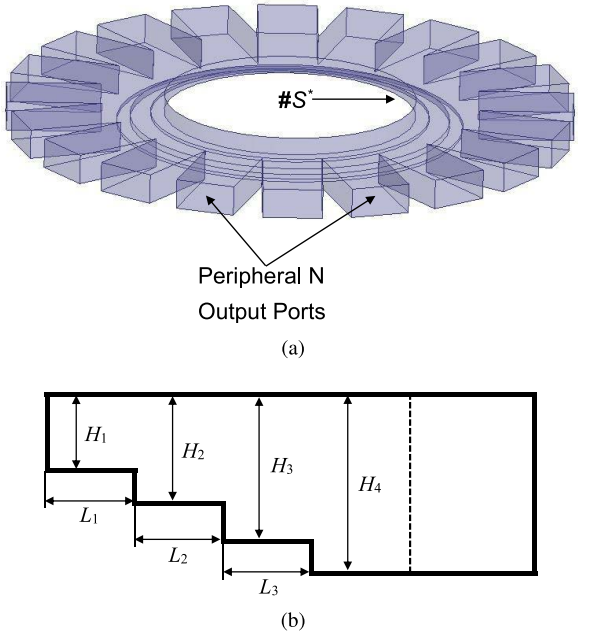

FIGURE 10. Stepped radial matching network comprising the N peripheral rectangular waveguide. (a) Three-dimensional view. (b) Side view.

synthesizer, the variation of its radius has little effect on the transmission performance, which makes it simple to design larger discs (corresponding to combinations with a larger number of ways). Based on the deduced generic impedance taper variation relationship, the taper profile can be quickly resolved when designing new synthesizers without the need to reuse the optimization of the 3-D EM simulator, which can significantly save design time.

B. THE STEPPED RADIAL MATCHING NETWORK AND PERIPHERAL RECTANGULAR WAVEGUIDE PORTS

The electromagnetic wave from the coaxial to radial waveguide transition is fed into the stepped radial matching network, and stimulates the desired TM_{00}-mode in the radial waveguide. Then, it is equally distributed to the peripheral N rectangular waveguides (WR-22: a = 5.69 mm, b = 2.845 mm). To suppress the higher order modes, the total radius of the matching network should be kept as small as possible, which can be specified by the following equation

$$R_r = \frac{a}{2\sin\left(\frac{\pi}{N}\right)} \tag{37}$$

In our design, $N = 20$, $Rr = 18.21$ mm.

The stepped radial matching network (comprising the N peripheral rectangular waveguide) can be modeled as a $N+1$ ports power division network with port $S*$ being a circular face at $r = r_t$. Ports 1 to N being rectangular waveguide ports, as shown in Fig. 10(a). In the previous analysis, we have known that the admittance at coaxial to radial waveguide transition out port is $Y_{in} = 1/Z_L$. Then, to obtain a perfect impedance match between the stepped network and the radial

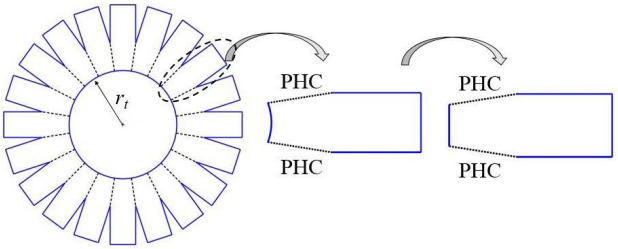

FIGURE 11. Schematic diagram of the simple electromagnetic model of the proposed power divider.

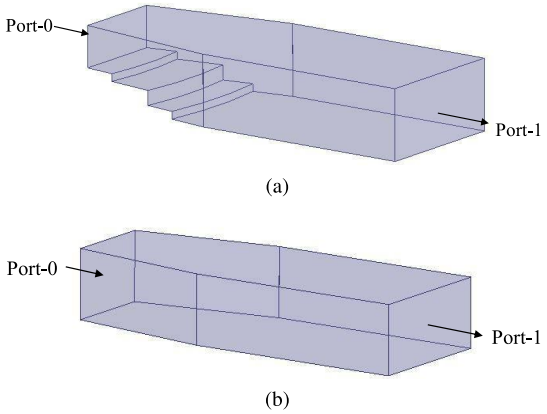

FIGURE 12. (a) Simplified two-port network with stepped matching element. (b) Simplified two-port network without the stepped matching element.

waveguide, the admittance at the port $S*$ must be satisfied:

$$Y_{\text{out}} = G_{\text{out}} + jB_{\text{out}} = Y_{\text{in}}^{*} \tag{38}$$

The simple electromagnetic model of the N-way stepped matching network is depicted in Fig. 11. Further, considering the radial symmetry of the power divider, the N+1-port network can be simplified to a two-port network for analysis, as shown in Fig. 12(a). Besides, to explain the operation principle of the network, an analogous network without the stepped matching have been given, as show in Fig. 12(b). The electromagnetic simulator HFSS was employed to simulate these two simplified networks, and the normalized input conductance of port-0 can be written as:

$$Y_0 = G_0 + jB_0 = \frac{1 - S_{00}}{1 + S_{00}} \tag{39}$$

where S_{00} is input reflection scattering parameter at port-0. Then, the condition of perfect matching is required to satisfy $G_0 = 1$ and $B_0 = 0$. However, parasitic inductance is inevitably induced at waveguide discontinuities, therefore, some capacitive steps are used in the radial matching network to achieve a reactance value of 1 at port 0. Consequently, broadband impedance matching can be achieved by optimizing the number and dimensions of the matching steps.

The optimized dimensions of the stepped radial matching network as follows: $H_1 = 1.926$ mm, $H_2 = 2.091$ mm, $H_3 = 2.679$ mm, $L_1 = 1.280$ mm, $L_2 = 3.235$ mm, and

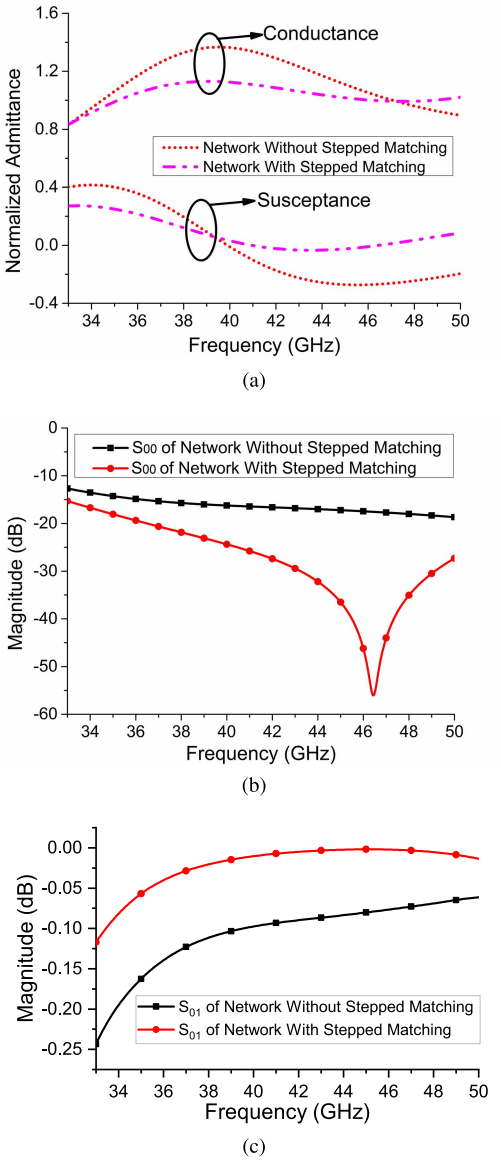

FIGURE 13. Simulated result comparison of two simplified two-port networks. (a) Input admittance of port-0. (b) Reflection coefficient at port-0. (c) Transmission coefficient.

$L_3 = 4.513$ mm. Fig. 13(a) shows the input admittance curves of the simplified two-port network. It can be seen that a flatter trend of the input admittance is achieved by adding a matching step, furthermore, the real and imaginary parts are stabilized around 1 and 0, respectively. In addition, the S-parameters shown in Fig. 13(b) and (c) indicate that the transmission efficiency of the two-port network is found to be significantly improved due to the addition of stepped matching elements.

C. COAXIAL TO RECTANGULAR WAVEGUIDE TRANSITION

To facilitate the application and measurement of millimeter wave systems, a transition from a coaxial waveguide to a standard rectangular waveguide is designed here, as shown

TABLE 2. Comparison with the radial power dividers reported over recent years.

Years/References	*Output type*	*Output way*	*Frequency range/Bandwidth*	*Return loss*	*Insertion loss*	*Amplitude/Phase imbalance*	*Robustness*
2009/[10]	Microstrip	10	11.5-16 GHz/30%	15 dB	0.8 dB	±1 dB/±5 deg	Not available
2012/[13]	Coaxial waveguide	8	520-1860 MHz/112%	12 dB	0.4 dB	±0.2 dB/±1 deg	Not available
2014/[23]	Coaxial waveguide	10	7.4-12 GHz/46%	18 dB	0.28 dB	±0.6 dB/±3 deg	Not available
2016/[14]	Coaxial waveguide	8	1.52-5.64 GHz/115%	22 dB	0.22 dB	±0.2 dB/±1.5 deg	Not available
2018/[31]	Coaxial waveguide	4	7.8-10.3 GHz/28%	18 dB	0.2 dB	±0.15 dB/±1.5 deg	Not available
2019/[32]	Rectangular waveguide	10	11-13 GHz/16.7%	25 dB	0.3 dB	±0.3 dB/±0.45 deg	Not available
2021/[33]	Ridge waveguide	5	3-5 GHz/50%	10 dB	0.5 dB	±0.2 dB/±0.5 deg	Not available
2021/[33]	Ridge waveguide	5	2.17-8.49 GHz/117%	15 dB	0.8 dB	±0.3 dB/±2.5 deg	Not available
2021/[34]	Rectangular waveguide	30	32-38 GHz/17%	15 dB	1 dB	±0.5 dB/±10 deg	Not available
2021/[35]	Rectangular waveguide	32	124-146 GHz/16.3%	10 dB	1.37 dB	-/-	Not available
This work	Rectangular waveguide	20	33-48 GHz/37%	20 dB	0.2 dB	±0.4 dB/±3 deg	High

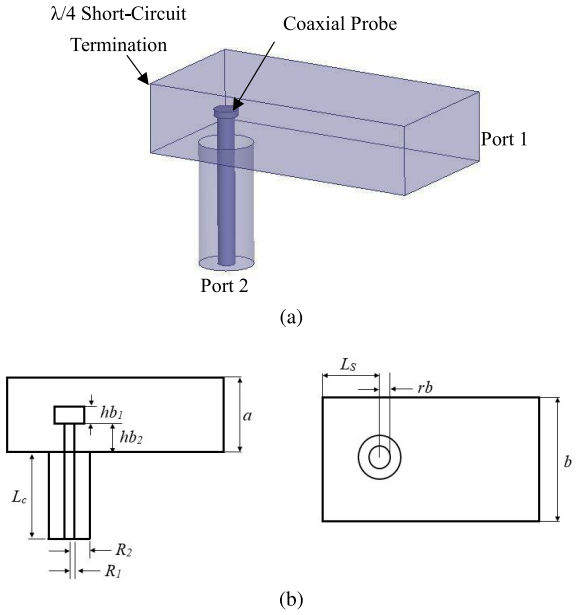

FIGURE 14. Transition structure of rectangular waveguide to coaxial waveguide. (a) Configuration. (b) Dimensional Parameters.

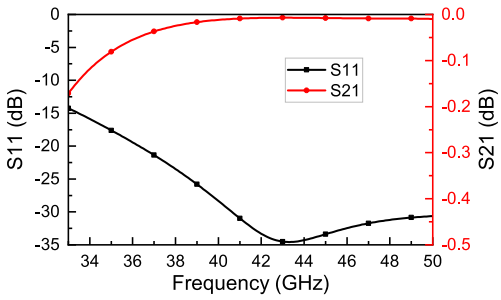

FIGURE 15. Optimized S-parameter of the rectangular to coaxial transition.

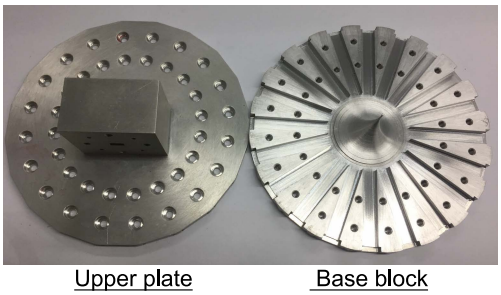

FIGURE 16. Prototype of a twenty-way waveguide power divider fabricated using CNC technology.

in Fig. 14. Specifically, the probe of the coaxial waveguide is inserted into the rectangular waveguide and is perpendicular to its E-plane. In addition, to prohibit the propagation of higher order modes within the transition, the radii of the inner and outer conductors of the coaxial waveguide should satisfy the following relationship, i.e:

$$R_1 + R_2 \leq c/\pi f_H. \tag{40}$$

where c is the light velocity, and f_H is the maximum operation frequency. In our design, $R_1 = 1.1$ mm, $R_2 = 0.35$ mm, and $L_c = 2$ mm. The optimized dimensions of the transition are $L_s = 1.779$ mm, $r_b = 0.493$ mm, $hb_1 = 0.257$ mm, and $hb_2 = 1.110$ mm. The simulation results of the transition are shown in Fig. 15, which shows better than 15 dB return loss and less than 0.2 dB insertion loss from 33 to 50 GHz.

D. SUMMARY OF THE STEP-BY-STEP DESIGN PROCEDURE

After the above analysis, the general design procedure can be summarized in the following specific steps.

1) Depending on the expected power divider application frequency range and (40) to determine the input and output rectangular waveguide dimensions (a, b), as well as coaxial waveguide dimensions (R_1, R_2).

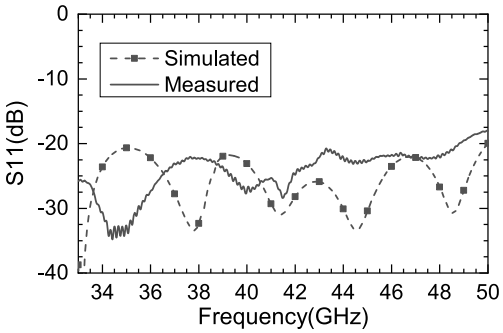

FIGURE 17. Simulated and measured reflection coefficient at the input rectangular port.

2) Based on the set number of power distribution paths N, the radius of the radial waveguide is selected according to (37).
3) Design the appropriate transition from coaxial to radial waveguide according to the approach discussed in Section II.
4) The N+1 port network is simplified to a two-port matching network, and then the dimensions of the stepped structure are optimized to match the input admittance over the operating frequency range ($G_0 = 1, B_0 = 0$).
5) Construct the transition from coaxial to rectangular waveguide, optimizing its dimensions to achieve the desired bandwidth and reflection coefficient.
6) Analyze the entire power divider with a field simulator to get the S-parameters at all the ports.

IV. MEASUREMENT RESULTS AND DISCUSSION

A prototype of a twenty-way radial waveguide power divider was fabricated, as shown in Fig. 16. Specifically, the power divider was simply divided into two aluminum plates (a lid and a base), which were implemented by a conventional CNC split-block fabrication process. The overall dimensions of the prototype are 106 mm × 106 mm ×40 mm.

The manufactured twenty-way power divider prototype was measured using an Agilent's vector network analyzer. Fig. 17 shows the simulated and measured input return loss of the power divider. It can be seen that the measured 20 dB-based return loss covers almost the entire Q-band (from 33 GHz to 48 GHz), which is in good agreement with the simulated results. The measured transmission characteristics of the fabricated power divider are shown in Fig. 18 (amplitude and phase are included). The results show that the average insertion loss is around 13.2 dB (including 13-dB power dividing inserting loss), and a maximum amplitude imbalance of ±0.4 dB and a phase imbalance of ±3° are achieved in the frequency range of 33-48 GHz.

Table 2 provides a summary which shows the comparison of the work presented in our article with some representative radial power dividers that have been published in recent years. First of all, it can be seen that many investigations

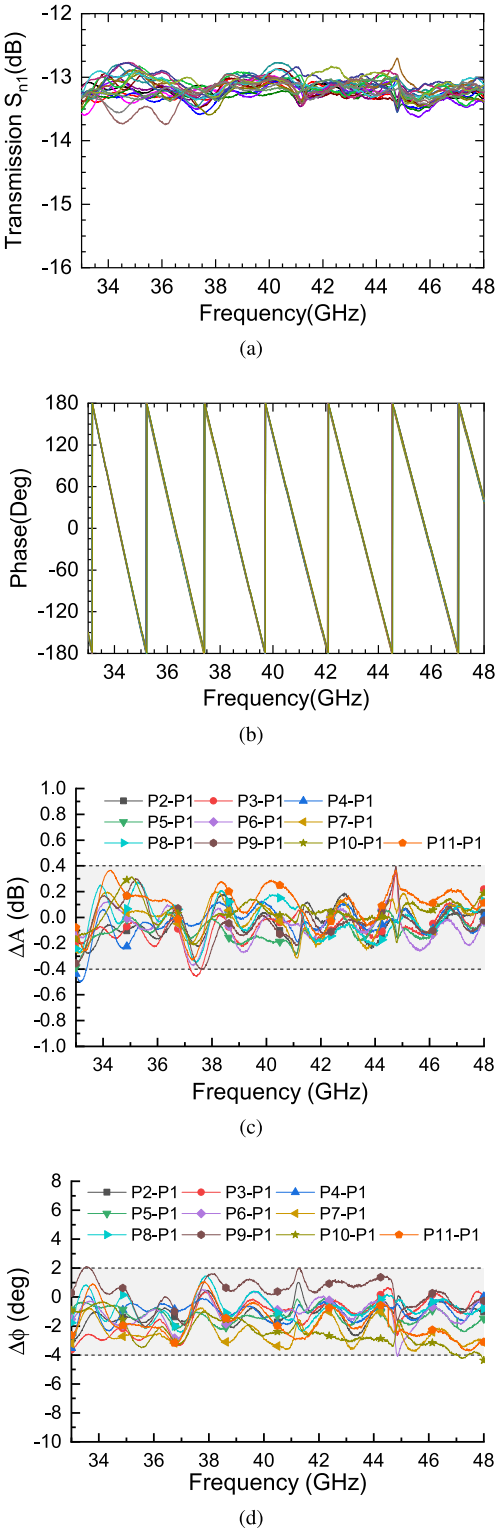

FIGURE 18. Measured transmission coefficient of the divider for all the twenty ports. (a) Amplitude. (b) Phase. (c) Amplitude imbalance. (d) Phase imbalance.

and developments of radial combiners are directed towards their operational bandwidth. In particular, the structures proposed in [13], [14] and [33], respectively, have relative

bandwidths even exceeding 100%. It owes to the radial transition configuration of its broadband on one hand and to the specificity of the output type (dominant mode is TEM mode or quasi-TEM mode) on the other hand. However, the extreme pursuit of bandwidth comes at the cost of degrading the power handling capability of the device, as it is difficult to adapt to high power applications, regardless of whether coaxial waveguides, microstrip lines or ridge waveguides are used as outputs. In addition, since these output configurations require additional assembly, this may lead to the fact that these radial synthesis solutions will suffer higher losses due to misalignment, etc., especially when the operating frequency increases to millimeter band. As can be seen from the table, most broadband radial combiners are concentrated in lower frequency bands, generally below the *X*-band.

On the other hand, some radial power synthesis solutions focusing on millimeter-wave applications have also been reported recently, as shown in Table 2. For example, in [34], a configuration for 30-way radial synthesis operating in the 32-38 GHz range was implemented by a proper combination of a rectangular waveguide Y-junction and a circular waveguide radial power divider. And in [35], a 32-way radial synthesizer was attained based on a simple coaxial-radial waveguide transition, which operates in the D-band. However, measurements on the sample showed that the former was found to have $\pm 10^{\circ}$ phase imbalance, while the latter suffered an insertion loss of up to 1.37 dB. This is mainly due to the lack of robustness of these devices, i.e., their RF performance is greatly affected by manufacturing tolerances and their severity.

The above comparison illustrates that the 20-way power divider with fully rectangular waveguide output proposed in this paper has good overall performance (covering the entire *Q*-band bandwidth, very low losses, and good amplitude/phase imbalance). In particular, it shows excellent robust performance in the range of millimeter waves, which is mainly attributed to the specially designed cycloidal-like transitions.

V. CONCLUSION

In this paper, a novel cycloidal-like taper transition from coaxial to radial waveguide is proposed. Detailed, transition profile curves have been synthesized in elaboration, which is based on the essential idea of impedance matching. The transition has several excellent properties, such as high power capacity (smooth profile), ultra-broadband, and excellent robustness. This makes it well suited for applications in millimeter-wave high-power multiplexed power synthesis networks. Therefore, a wideband twenty-way waveguide power divider was designed, fabricated, and measured to validate the proposed solution. Experimental results show that the fabricated prototype achieves very low insertion loss and good amplitude phase characteristics across the entire *Q*-band as expected. In addition, it is worth mentioning that the proposed method is potentially scalable to more power synthesis, which only requires the design of a larger radius transition structure.

REFERENCES

[1] K. J. Russell, "Microwave power combining techniques," *IEEE Trans. Microw. Theory Techn.*, vol. MTT-27, no. 5, pp. 472–478, May 1979, doi: 10.1109/TMTT.1979.1129651.

[2] K. Chang and C. Sun, "Millimeter-wave power-combining techniques," *IEEE Trans. Microw. Theory Techn.*, vol. MTT-31, no. 2, pp. 91–107, Feb. 1983, doi: 10.1109/TMTT.1983.1131443.

[3] Q. Xue, K. Song, and C. H. Chan, "China: Power combiners/dividers," *IEEE Microw. Mag.*, vol. 12, no. 3, pp. 96–106, May 2011, doi: 10.1109/MMM.2011.940320.

[4] L. Guo, J. Li, W. Huang, H. Shao, T. Ba, T. Jiang, Y. Jiang, and G. Deng, "A waveguide magic-T with coplanar arms for high-power solid-state power combining," *IEEE Trans. Microw. Theory Techn.*, vol. 65, no. 8, pp. 2942–2952, Aug. 2017, doi: 10.1109/TMTT.2017.2661741.

[5] L. W. Epp, D. J. Hoppe, A. R. Khan, and S. L. Stride, "A high-power-band (31–36 GHz) solid-state amplifier based on low-loss corporate waveguide combining," *IEEE Trans. Microw. Theory Techn.*, vol. 56, no. 8, pp. 1899–1908, Aug. 2008, doi: 10.1109/TMTT.2008.927299.

[6] L. Guo, J. Li, W. Huang, H. Shao, T. Ba, S. Xie, Y. Jiang, and G. Deng, "Design of compact high-isolation four-way power combiners," *IEEE Trans. Microw. Theory Techn.*, vol. 66, no. 5, pp. 2185–2198, May 2018, doi: 10.1109/TMTT.2018.2812175.

[7] L. A. Li, B. J. Hilliard, J. R. Shafer, J. Daggett, E. J. Dickman, and J. P. Becker, "A planar compatible traveling-wave waveguide-based power divider/combiner," *IEEE Trans. Microw. Theory Techn.*, vol. 56, no. 8, pp. 1889–1898, Aug. 2008, doi: 10.1109/TMTT.2008.926555.

[8] Q. X. Chu, Z. Y. Kang, Q. S. Wu, and D. Y. Mo, "An in-phase output Ka-band traveling-wave power divider/combiner using double ridgewaveguide couplers," *IEEE Trans. Microw. Theory Techn.*, vol. 61, no. 9, pp. 3247–3253, Sep. 2013, doi: 10.1109/TMTT.2013.2273764.

[9] K. Song and Q. Xue, "Ultra-wideband ring-cavity multiple-way parallel power divider," *IEEE Trans. Ind. Electron.*, vol. 60, no. 10, pp. 4737–4745, Oct. 2013, doi: 10.1109/TIE.2012.2208441.

[10] K. Song and Q. Xue, "Planar probe coaxial-waveguide power combiner/divider," *IEEE Trans. Microw. Theory Techn.*, vol. 57, no. 11, pp. 2761–2767, Nov. 2009, doi: 10.1109/TMTT.2009.2032483.

[11] S. Hu, K. Song, and Y. Fan, "Compact quasi-planar broadband rectangular ring-cavity power divider using inserted ground waveguide probe," *Electron. Lett.*, vol. 52, no. 8, pp. 628–630, Apr. 2016, doi: 10.1049/el.2015.3763.

[12] P. Jia, L.-Y. Chen, A. Alexanian, and R. A. York, "Multioctave spatial power combining in oversized coaxial waveguide," *IEEE Trans. Microw. Theory Techn.*, vol. 50, no. 5, pp. 1355–1360, May 2002, doi: 10.1109/22.999150.

[13] M. Amjadi and E. Jafari, "Design of a broadband eight-way coaxial waveguide power combiner," *IEEE Trans. Microw. Theory Techn.*, vol. 60, no. 1, pp. 39–45, Jan. 2012, doi: 10.1109/TMTT.2011.2171499.

[14] R. D. Beyers and D. I. L. de Villiers, "A general impedance tapered transition for N-way conical and coaxial combiners," *IEEE Trans. Microw. Theory Techn.*, vol. 64, no. 12, pp. 4482–4490, Dec. 2016, doi: 10.1109/TMTT.2016.2623624.

[15] K. J. Song, F. Zhang, S. Y. Hu, and Y. Fan, "Ku-band 200-W pulsed power amplifier based on waveguide spatially power-combining technique for industrial applications," *IEEE Trans. Ind. Electron.*, vol. 61, no. 8, pp. 4274–4280, Aug. 2014, doi: 10.1109/TIE.2013.2284137.

[16] Y.-P. Hong, D. F. Kimball, P. M. Asbeck, J.-G. Yook, and L. E. Larson, "Single-ended and differential radial power combiners implemented with a compact broadband probe," *IEEE Trans. Microw. Theory Techn.*, vol. 58, no. 6, pp. 1565–1572, Jun. 2010, doi: 10.1109/TMTT.2010.2049165.

[17] T.-I. Hsu and M. D. Simonutti, "A wideband 60 GHz 16-way power divider/combiner network," in *IEEE MTT-S Int. Microw. Symp. Dig.*, May 1984, pp. 175–177, doi: 10.1109/MWSYM.1984.1131729.

[18] J. Schellenberg and M. Cohn, "A wideband radial power combiner for FET amplifiers," in *IEEE ISSCC Tech. Dig. Papers*, Feb. 1978, pp. 164–165, doi: 10.1109/ISSCC.1978.1155840.

[19] G. W. Swift and D. I. Stones, "A comprehensive design technique for the radial wave power combiner," in *IEEE MTT-S Int. Microw. Symp. Dig.*, May 1988, pp. 279–281, doi: 10.1109/MWSYM.1988.22030.

[20] K. Song, Y. Fan, and Z. He, "Broadband radial waveguide spatial combiner," *IEEE Microw. Wireless. Compon. Lett.*, vol. 18, no. 2, pp. 73–75, Feb. 2008, doi: 10.1109/LMWC.2007.911984.
[21] A. E. Fathy, S.-W. Lee, and D. Kalokitis, "A simplified design approach for radial power combiners," *IEEE Trans. Microw. Theory Techn.*, vol. 54, no. 1, pp. 247–255, Jan. 2006, doi: 10.1109/TMTT.2005.860302.
[22] J.-C.-S. Chieh, M. Civerolo, and A. Clawson, "A ultra wideband radial combiner for X/Ku-band using CNC and DMLS processes," *IEEE Microw. Wireless Compon. Lett.*, vol. 25, no. 5, pp. 286–288, May 2015, doi: 10.1109/LMWC.2015.2409806.
[23] R. D. Beyers and D. I. L. de Villiers, "Compact conical-line power combiner design using circuit models," *IEEE Trans. Microw. Theory Techn.*, vol. 62, no. 11, pp. 2650–2658, Nov. 2014, doi: 10.1109/TMTT.2014.2359855.
[24] D. I. L. de Villiers, P. W. van der Walt, and P. Meyer, "Design of a ten-way conical transmission line power combiner," *IEEE Trans. Microw. Theory Techn.*, vol. 55, no. 2, pp. 302–308, Feb. 2007, doi: 10.1109/TMTT.2006.890065.
[25] D. I. L. de Villiers, P. W. van der Walt, and P. Meyer, "Design of conical transmission line power combiners using tapered line matching sections," *IEEE Trans. Microw. Theory Techn.*, vol. 56, no. 6, pp. 1478–1484, Jun. 2008, doi: 10.1109/TMTT.2008.923879.
[26] R. D. Beyers and D. I. L. de Villiers, "Design and analysis of an impedance tapered conical to coaxial transmission line transition," in *Proc. 44th Eur. Microw. Conf.*, Oct. 2014, pp. 307–310, doi: 10.1109/EuMC.2014.6986431.
[27] Q.-X. Chu, D.-Y. Mo, and Q.-S. Wu, "An isolated radial power divider via circular waveguide TE_{01}-mode transducer," *IEEE Trans. Microw. Theory Techn.*, vol. 63, no. 12, pp. 3988–3996, Dec. 2015, doi: 10.1109/TMTT.2015.2495204.
[28] J. R. Montejo-Garai, J. A. Ruiz-Cruz, and J. M. Rebollar, "A 10-way power divider based on a transducer and a radial junction operating in the circular TM_{01} mode," *IEEE Access*, vol. 7, pp. 127353–127361, 2019, doi: 10.1109/ACCESS.2019.2939291.
[29] M. E. Bialkowski and V. P. Waris, "Analysis of an N-way radial cavity divider with a coaxial central port and waveguide output ports," *IEEE Trans. Microw. Theory Techn.*, vol. 44, no. 11, pp. 2010–2016, Nov. 1996.
[30] N. Marcuvitz, *Waveguide Handbook*. New York, NY, USA: McGraw-Hill, 1951.
[31] L. Guo, J. Li, W. Huang, H. Shao, and T. Ba, "Design of a high-isolation n-way power combiner based on a 2n + 1 port mode network," *IEEE Access*, vol. 6, pp. 6446–6454, 2018, doi: 10.1109/ACCESS.2017.2786472.
[32] J. R. Montejo-Garai, J. A. Ruiz-Cruz, and J. M. Rebollar, "A 10-way power divider based on a transducer and a radial junction operating in the circular TM_{01} mode," *IEEE Access*, vol. 7, pp. 127353–127361, 2019, doi: 10.1109/ACCESS.2019.2939291.
[33] M. M. Fahmi, J. A. Ruiz-Cruz, and R. R. Mansour, "Design of ridge waveguide radial combiners," *IEEE Trans. Microw. Theory Techn.*, vol. 70, no. 1, pp. 895–906, Jan. 2022, doi: 10.1109/TMTT.2021.3120732.
[34] Z. Ma, X. Xie, Y. Xu, X. Li, and Z. Yan, "A Ka-band 30-way radial power divider with Y-junctions," in *Proc. Int. Conf. Microw. Millim. Wave Technol. (ICMMT)*, May 2021, pp. 1–3, doi: 10.1109/ICMMT52847.2021.9618129.
[35] X. Deng, Y. Rao, K. Huang, J. Zhou, W. Su, and X. Luo, "A high efficiency D-band 32-channel radial waveguide power divider/combiner," in *IEEE MTT-S Int. Microw. Symp. Dig.*, Jun. 2021, pp. 566–569, doi: 10.1109/IMS19712.2021.9574842.

FEI LIANG received the M.S. degree from Sichuan University, Chengdu, China. He is currently working with the Second Research Institute of Civil Aviation Administration of China (CAAC), Chengdu. His research interests include air traffic control technology, aerospace metamaterials, and high-power microwave and millimeter-wave components and circuits.

JIAQUAN YE received the M.S. degree. He is currently working with the Second Research Institute of Civil Aviation Administration of China (CAAC), Chengdu, China. His research interests include air traffic control technology and aviation metamaterials.

YUANKAI LI received the M.S. degree from the University of Electronic Science and Technology of China, Chengdu, China. She is currently working with the Second Research Institute of Civil Aviation Administration of China (CAAC), Chengdu. Her research interests include aviation navigation theory, radio communication, and aviation metamaterials technology.

HUAN LIN received the graduate degree from the Civil Aviation Flight University of China, Guanghan, Sichuan. She is currently working with the Second Research Institute of Civil Aviation Administration of China (CAAC), Chengdu, China. Her research interests include electromagnetic environment assessment of ATC navigation equipment and air traffic control technology.

BIN YUAN received the M.S. degree from the University of Electronic Science and Technology of China, Chengdu, China. He is currently working with the Second Research Institute of Civil Aviation Administration of China (CAAC), Chengdu. His research interests include civil aviation air traffic control technical support and electromagnetic environment assessment.

JIAN XU received the M.S. degree from Sichuan University, Chengdu, China. He is currently working with the Second Research Institute of Civil Aviation Administration of China (CAAC), Chengdu. His research interest includes air traffic control technology.